Water Management in PEM Fuel Cells

Peter Berg,[a] Keith Promislow,[a,z] Jean St. Pierre,[b] Jürgen Stumper,[b,*] and Brian Wetton[c]

[a]*Department of Mathematics, Simon Fraser University, Burnaby V5A 1S6, Canada*
[b]*Ballard Power Systems, Burnaby V5J 5J9, Canada*
[c]*Department of Mathematics, University of British Columbia, Vancouver V6T 1Z2, Canada*

A simplified model for water management in a polymer electrolyte membrane (PEM) fuel cell operating under prescribed current with iso-potential plates is presented. The consumption of gases in the flow field channels, coupled to the electric potential and water content in the polymer membrane, is modeled in a two-dimensional slice from inlet to outlet and through the membrane. Both co- and counter-flowing air and fuel streams are considered, with attention paid to sensitivity of along-the-channel current density to inlet humidities, gas stream composition, and fuel and oxygen stoichiometries. The parameters describing the nonequilibrium kinetics of the membrane/catalyst interface are found to be fundamental to accurate fuel cell modeling. A new parameter which models nonequilibrium membrane water uptake rates is introduced. Four parameters, the exchange current, a membrane water transfer coefficient, an effective oxygen diffusivity, and an average membrane resistance, are fit to a subset of data and then held constant in subsequent runs which compare polarization curves, current density and membrane hydration distributions, water transfer, and stoichiometric sensitivity to the balance of the experimental data.
© 2004 The Electrochemical Society.   [DOI: 10.1149/1.1641033] All rights reserved.

Polymer electrolyte membrane (PEM) fuel cells (FCs) are complicated devices typically modeled by arrays of equations describing consumption and transport of reactant gases, humidification levels of the membrane, cell voltage, current production, and multiphase multispecies heat and mass transport in the gas diffusion areas.[1-12] All-encompassing models have the advantage of completeness and can hope for accuracy, but their complexity confounds the process of determining cause and effect relationships. This article presents a simplified model which captures the essential features of over-all FC performance: consumption of reactants along the flow-field channels, water transfer between anode and cathode, hydration levels within the membrane, mass transport limitations in the gas diffusion and catalyst layers, and water transport into and out of the polymer membrane. The high aspect ratio (AR) of automotive scale PEM FC reactors, roughly 10000:1 down-the-channel verses through-the-membrane, motivates consideration of a two-dimensional (2-D) along-the-channel and through-the-membrane model coupling 1-D water and proton transport to the fast flow in the channels. Numerical results are compared to experimental data at a variety of operational conditions, including high and low stoichiometric inlet fluxes, low dew-point inlets, co- and counter-flowing fuel and air streams. The simplicity of the model facilitates the identification of key, rate-limiting features of the FC operation which are essential to efficient operation. Although it is not considered here, the model is readily extendible to a full-stack simulation.

The proton conductivity of Nafion and related perfluorinated sulfonic polymers is excellent when fully hydrated, but falls with decreasing water content. Management of the water content in the membrane is a key to efficient FC operation. The mechanisms of membrane dehydration are (*i*) electro-osmotic drag pulling water from anode to cathode, and (*ii*) loss of water to undersaturated fuel or air streams. There is a considerable literature on the first mechanism, which focuses primarily on the water transport mechanism within the membrane, assuming either a diffusive mechanism[9] or a convective one based upon phenomenologically determined capillary pressure isotherms.[4] In practical applications the dry anode issue has been addressed by the use of thin 25-50 μm membranes which facilitate the back diffusion of water, rehydrating the anode. However the very thinness of these membranes exacerbates the second effect, which is further complicated by the desire to remove or diminish dependency on on-board humidification of gas streams. While the electro-osmotic drag is a bulk effect in the membrane, the loss of water to channel streams requires a characterization of the membrane's capacity to retain its water. Cell performance is well known to be sensitive to the composition of the catalyst layer, one aspect of which is its strong hydrophobicity. The numerical and experimental data presented herein suggest that the membrane's hydrophilic nature, in contrast to the hydrophobicity of the sublayer including the catalyst load, play a key role in water management, acting to seal water inside the membrane. Other factors, such as gas diffusion layer thickness and porosity play a significant, but secondary, role.

Previous water management models have imposed the equilibrium water sorption value, a function of local water activities, as the water content of the boundary of the membrane.[4,9,13] However, the time scale for a membrane to reach its equilibrium sorption state is on the order of 100-1000 s when placed in humid air,[13,14] while water production associated with a current of 1 A/cm² is sufficient to completely hydrate a dry 50 μm thick Nafion 112 membrane in roughly 10 s. Rather than making an equilibrium assumption on the water content, the flux of water into and out of the membrane is assumed to be proportional to the difference between the local water content and equilibrium sorption values. The proportionality constant governing the membrane water transfer characterizes the porosity and hydrophilic-hydrophobic nature of the membrane/catalyst layer interface, and to a lesser extend the role of the gas diffusion layer.

The model presented has four key fitted parameters: exchange current, membrane water transfer coefficient, an effective oxygen diffusivity, and an average membrane resistance. Each of these parameters characterizes a fundamental, distinct rate process. These four parameters are fit to a small subset of the data, and then held constant in comparisons of computational results to the balance of the data set. Within the framework of the model, cause and effect relations are built up from comparisons of the fit values of these parameters for different classes of data.

This paper is organized as follows, in the Model section the model equations for the bulk motion within each component and the major limiting assumptions are presented. The Interface conditions section contains the interface conditions which interrelate the components. In the section on Model reduction, experimental details, and fitting, the membrane model is explicitly reduced to a single nonlinear voltage balance equation, the experimental details and the fitting procedure for the four cell parameters are presented. The Results and discussion section contains results.

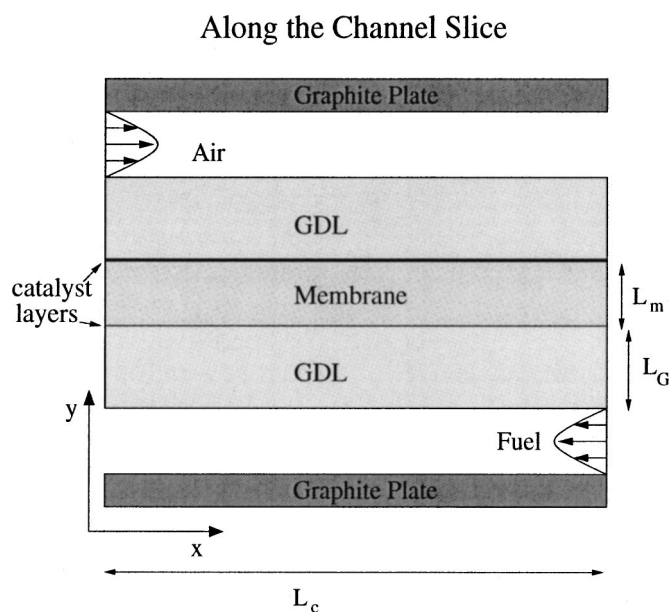* Electrochemical Society Active Member.
z E-mail: kpromisl@sfu.ca

Along the Channel Slice

Figure 1. A schematic overview of the 2D unit cell for counterflow. In coflow, the fuel flows from left to right. Coolant flows in same direction as air in both cases.

The Model

The model is based upon a 2-D slice running from inlet to outlet along a single channel and through the membrane from the cathode channel to the anode channel, as outlined in Fig. 1. Emphasis is given to the following processes within the unit cell: along-the-channel variation in gas composition within the gas streams, oxygen transport from the cathode gas stream to the catalyst sites, water transfer between the membrane and the gas streams, current generation at the catalyst sites, and water and voltage distributions within the membrane. For both co- and counter-flowing fuel and air streams, along-the-channel current generation, cathode to anode water transfer, and channel water drop-out are investigated as functions of inlet humidification and stoichiometry. The high AR of the domain, roughly a meter for the channel length against 100 μm for the membrane-electrode assembly (MEA) motivates restricting local membrane transport to the y direction, taking the channel flux solely in the x direction. Membrane concentrations vary along the channel through the interfacial conditions coupling them to the channel gas composition. The channel fluxes are taken to be 1-D, *i.e.*, the channel is well mixed. This $(1 + 1)$-dimensional model represents a collection of 1-D slices for the membrane, strongly coupled by the channel flow. This model is similar in spirit to that proposed in Ref. 8. The temperature profile is assumed to be dominated by the coolant streams, and is taken to be a prescribed function of x only. As in the experimental setups from which the data is taken, the total current produced is prescribed, while the bipolar plates are isopotential. Tables I and II list the variables and constants associated with the model. As a convention, all positive membrane fluxes point from anode to cathode, positive channel fluxes are from respective inlet to outlet.

Assumptions.—The main approximations are summarized below:

1. $(1 + 1)$-dimensional model: In the channel, a 1-D transport model is considered which accounts only for mass exchange with the membrane and convective transport. The membrane model includes transport along the y axis between cathode and anode. Variations in x arise in the membrane through coupling to the channel.

2. Temperature throughout the unit cell is a prescribed linear function of x only, from T_{in} at the air inlet ($x = 0$) to T_{out} at the air outlet ($x = L_c$).

3. The gases in the channel are governed by the ideal gas law. Variations of channel gas concentrations in the y coordinate are neglected. The gas pressure is assumed constant from inlet to outlet.

4. The gas diffusion layer (GDL) is only modeled in terms of mass transport coefficients which relate the concentrations of oxygen and water vapor at the membrane to their channel values and their fluxes.

5. Ohmic losses in the GDL and graphite plate are neglected. The anode overpotential loss is neglected.

6. Catalyst layers are treated as interfaces.

7. In the membrane, only water and hydronium are considered, an effective water drag coefficient of one is assumed.

8. The FC is at steady state and is driven at constant total current I_T at prescribed anode and cathode stoichiometries, S_a and S_c, respectively.

The channel model.—The variables in the cathode channel are oxygen, vapor, and nitrogen concentrations, $C_c = (C_{c,1}, C_{c,2}, C_{c,3})$ respectively. At the air inlet, $x = 0$, the corresponding molar fluxes $Q_c(0)$, and the inlet pressure $P_c(0)$ are prescribed, from which the channel variations of the fluxes, concentrations, and mixture velocity $Q_c(x)$, $C_c(x)$, and $V_c(x)$ are determined. For the anode channel, the variables are hydrogen and water vapor concentrations $C_a = (C_{a,1}, C_{a,2})$. $Q_{c,i}$ and $Q_{a,i}$ are molar fluxes per cross plane distance. The anode inlet is at $x_a = 0$ for coflow and at $x_a = L_c$ for counter flow, where the molar fluxes $Q_a(x_a)$ and mixture pressure, $P_{a,in}$, are prescribed. The molar fluxes of hydrogen and oxygen at the inlets, $Q_{a,1}(x_a)$ and $Q_{c,1}(0)$, are given through their respective stoichiometries, $S_c, S_a \geq 1$, in terms of the total current I_T as

$$Q_{a,1}(x_a) = S_a \frac{I_T}{2F} \qquad [1]$$

$$Q_{c,1}(0) = S_c \frac{I_T}{4F} \qquad [2]$$

Along the channel flux.—The main computed along-the-channel quantities are the local current density $I(x)$ and the total anode to cathode water flux $J_w^T = J_w + J_+ = J_w + I/F$ (see the Model section on Polymer electrolyte membrane). The membrane water transfer $\alpha = \alpha(x)$, measures the water crossing from anode to cathode as a function of the water production in the cathode catalyst layer. It is written in terms of $I(x)$ and $J_w^T(x)$ as

$$\alpha = \frac{2F J_w^T}{I} \qquad [3]$$

At steady state, conservation of mass implies that the variation of the molar fluxes in terms of the oxygen flux $Q_{c,1}$ and water flux $Q_{c,2}$ are controlled by the local current and water transfer

$$\frac{dQ_{c,1}}{dx} = -\frac{I L_w}{4F} \qquad [4]$$

$$\frac{dQ_{c,2}}{dx} = (1 + \alpha) \frac{I L_w}{2F} \qquad [5]$$

while the nonreactive $Q_{c,3}$ is constant in x. The term $(1 + \alpha)$ in (Eq. 5) reflects the combined contributions of water production and water transfer. These equations are combined with the prescribed inlet values at $x = 0$ to compute Q_c along the length of the channel.

The molar concentrations.—The cases of undersaturated and saturated water vapor must be differentiated to determine the local molar concentrations C_c and mixture velocity $V_c(x)$ as functions of the fluxes Q_c and the channel pressure, P_c.

For the undersaturated case: The O_2 and N_2 fluxes are carried at the gas velocity V_c, so

Table I. An overview of the model variables.

RH	Relative humidity in per cent
T	Temperature profile along the channel in Kelvin
U_{mod}	Computed external voltage in V
V_a	Average anode channel gas velocity in m/s
V_c	Average cathode channel gas velocity in m/s
α	Membrane water transfer coefficient (dimensionless)
α_T	Total water transfer (dimensionless)
η_a	Anode overpotential in V
η_c	Cathode overpotential in V
ϕ	Membrane electric potential in V
ϕ_m	Membrane electric losses in V
σ	Effective membrane conductivity in S cm^{-2}
$\bar{\sigma}$	Effective average membrane conductivity in S cm^{-2}
$a = 1200$ mol/m^3	Fixed charge (sulfonic acid groups) concentration
$A_c = 1 \times 10^{-6}$ m^3	Channel cross-sectional area
$A_{\text{eff}} = 300$ cm^2	Effective MEA area
$c_w^{\text{max}} = 14a$	Maximum sorption equilibrium water content
$C_o^{\text{ref}} = 9.60$ mol/m^3	Cathode oxygen reference concentration
$d_c = 1.36$ mm	Distance between channels
$D_+(c_w,T) = d_+ \exp(-1683/T)c_w$	Hydronium diffusion coefficient, m^2/s
$d_+ = 1.6 \times 10^{-8}$ m^2/s	Hydronium diffusion coefficient
$D_w/(c_w,T) = d_w \exp(-2436/T)c_w$	Water diffusion coefficient, m^2/s
$d_w = 2.1 \times 10^{-7}$ m^2/s	Water diffusion coefficient
D	Water diffusion constant, m^2/s
E_o	Open circuit potential, V
$F = 96500$ C/mol	Faraday constant
$h_c = 1$ mm	Width and height of channel
$H_0 = -52300$ J/mol	Enthalpy of hydronium formation[10]
$H_o = 2 \times 10^5$ atm cm^3/mol	Henry's constant for oxygen
$i_{o,a}$	Anode exchange current density, A/cm^2
$i_{o,c}$	Cathode exchange current density, A/cm^2
I_T	Total current, A
$K_e(T)$, $K_0 = 6.2$	Ion exchange equilibrium constant[10] (dimensionless)
$L_c = 0.67$ m	Channel length
$L_m = 50$ μm	Membrane thickness
$L_w = 1$ mm	Width of MEA associated with one channel
$L_G = 250$ μm	Thickness of GDL
$n = 36$	Number of channels in the span-wise direction
$N = 1$	Water drag coefficient
$P_{a,\text{in}}$	Anode inlet pressure, Pa
$P_{c,\text{in}}$	Cathode inlet pressure, Pa
$P_{a,\text{in}}^w$	Water partial pressure at anode inlet, Pa
$\mathcal{R} = 8.31$ J K^{-1} mol^{-1}	Gas constant
S_a	Anode stoichiometry (dimensionless)
S_c	Cathode stoichiometry (dimensionless)
T_{in}	Coolant inlet temperature, K
T_{out}	Coolant outlet temperature, K
$T_{a,\text{in}}$	Anode inlet temperature, K
$T_{a,\text{out}}$	Anode outlet temperature, K
$T_{c,\text{in}}$	Cathode inlet temperature, K
$T_{c,\text{out}}$	Cathode outlet temperature, K
$T_{\text{dew,a}}$	Dew point of anode inlet gas
$T_{\text{dew,c}}$	Dew point of cathode inlet gas

Table II. An overview of the model parameters and functional relations.

U	External voltage in V
U_{exp}	Measured external voltage in V
α_c	Cathode transfer coefficient
$\bar{\gamma} = 5.7 \times 10^{-6}$ m/s	Water mass transfer coefficient
δ	Oxygen mass transfer coefficient in s mole m^{-1} C^{-1}

$$V_c A_c C_{c,1} = Q_{c,1} \qquad [6]$$

$$V_c A_c C_{c,3} = Q_{c,3} \qquad [7]$$

If the water vapor is undersaturated, then the water flux is also carried at the same gas velocity

$$V_c A_c C_{c,2} = Q_{c,2} \qquad [8]$$

The ideal gas law and Dalton's law yield

$$P_c = \mathcal{R}T(C_{c,1} + C_{c,2} + C_{c,3}) \qquad [9]$$

where $T(x)$ is the prescribed channel gas temperature. The four Eq. 6-9 yield expressions for the mixture concentrations

$$C_{c,j} = \frac{P_c}{\mathcal{R}T} \frac{Q_{c,j}}{Q_{c,1} + Q_{c,2} + Q_{c,3}} \quad j = 1,2,3 \qquad [10]$$

If the vapor pressure, given by $P_2 = \mathcal{R}TC_{c,2}$, is less than the saturation pressure $P_{sat}(T)$, our relations are self-consistent. If, however, the predicted vapor pressure is greater than the saturation pressure, it is recomputed as below.

For the saturated case: Replace (Eq. 8) with a saturation assumption

$$C_{c,2} = P_{sat}(T)/\mathcal{R}T \qquad [11]$$

and obtain

$$C_{c,j} = \frac{P_c - P_{sat}(T)}{\mathcal{R}T} \frac{Q_{c,j}}{Q_{c,1} + Q_{c,3}} \quad j = 1,3 \qquad [12]$$

The value of V_c can be calculated from Eq. 7. The water flux carried in liquid form is given by

$$Q_{c,1} = Q_{c,2} - V_c A_c P_{sat}(T)/\mathcal{R}T \qquad [13]$$

Anode channel.—In the anode gas channels, proceeding as in the model sections Along the channel flux and Molar concentrations the hydrogen and water flux satisfy

$$\frac{dQ_{a,1}}{dx} = \pm\frac{IL_w}{2F} \qquad [14]$$

$$\frac{dQ_{a,2}}{dx} = \pm\alpha\frac{IL_w}{2F} \qquad [15]$$

where the $+$ sign is taken in Eq. 14,15 for counterflow and the $-$ sign for coflow. These conservation laws reflect the local consumption of hydrogen at the catalyst layers and the water transfer α from anode to cathode. For counterflow, the inlet values are prescribed at $x = L_c$ for the anode channel, and integration is from $x = L_c$ to $x = 0$. The remainder of the formulation is identical to the cathode case, including undersaturated and saturated cases.

The PEM.—The main feature of a proton exchange membrane is the equilibrium between the local water content, the protons bound to the fixed charge (acid) groups, and the mobile protons dissolved in the water, which form complexes with surrounding water molecules. In its simplest form, the ion exchange equilibrium arises from Reaction 10

$$SO_3^-H^+ + H_2O \rightleftharpoons SO_3^- + H_3O^+ \qquad [16]$$
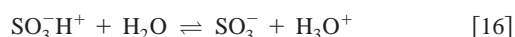
At equilibrium, the concentration of bound protons $c_b = [SO_3H]/a$, as normalized by the sulfonic acid group concentration $a = [SO_3^-] + [SO_3H]$, is determined by the hydronium concentration $c_+ = [H_3O^+]/a$, and the local free water content $c_w = [H_2O]/a$, via

$$c_b c_w K_e(T) = c_+(1 - c_b) \qquad [17]$$

where the equilibrium constant depends sensitively on temperature[10]

$$K_e(T) = K_0 \exp\left[-\frac{H_0}{\mathcal{R}}\left(\frac{1}{T} - \frac{1}{298}\right)\right] \qquad [18]$$

The assumption of local electroneutrality (LEN)[15] requires

$$1 - c_b - c_+ = 0 \qquad [19]$$

which together with Eq. 17 relates the ion concentration to the water concentration and temperature

$$c_+(c_w,T) = -\frac{K_e c_w}{2} + \sqrt{\left(\frac{K_e c_w}{2}\right)^2 + K_e c_w} \qquad [20]$$

The membrane water content determines the hydronium concentration, and hence the total water concentration $c_T = c_w + c_+$, as a function of temperature.

The nature of the mechanism for transport of water and charge within the membrane is a subject of some debate. On the one hand there are Nernst-Planck equations,[15] derived from a diffusive mechanism in the membrane using a dusty-gas model based upon the Maxwell-Stefan equations[10] for the flux of free water and hydronium. On the other hand are transport equations derived from a convective model with pressure gradients arising from a combination of capillary pressure and elastic stresses due to membrane swelling.[4] However, in these later models, the capillary pressure, p_{cap}, is prescribed as a function of the local water content through the capillary isotherm $c_w = f(p_{cap})$, which, through a Darcy law relation, gives transport equations of a functional form similar to that of the diffusive formulation.

Our treatment follows the diffusive model proposed by Thampan *et al.*[10] Assuming that only hydronium and free water are present in the membrane, and neglecting frictional effects between the two species which can lead to pumping action of water at high water concentrations,[16] leads to an electro-osmotic drag coefficient of $N = 1$, comparable to experimentally measured values of 1-1.4 (see Ref. 17,18) for membrane hydration levels $c_w \leqslant 15$ considered here. These assumptions lead to the following Nernst-Planck equations for the hydronium and free water flux

$$-D_+ \frac{dc_+}{dy} - \frac{F}{\mathcal{R}T}D_+ c_+ \frac{d\phi}{dy} = J_+/a \qquad [21]$$

$$-D_w \frac{dc_w}{dy} = J_w/a \qquad [22]$$

Note that inclusion of a water-content dependent drag coefficient, $N(c_w)$, results in an additive term $[N(c_w) - 1]J_+/a$ on the left-hand side of Eq. 22.

The assumption of 1-D transport in the membrane implies that the fluxes J_+ and J_w are independent of y. The diffusion coefficients are based on literature values[1,19]

$$D_+(c_w,T) = d_+ \exp(-1683/T)c_w \qquad [23]$$

$$D_w(c_w,T) = d_w \exp(-2436/T)c_w \qquad [24]$$

where $d_+ = 1.6 \times 10^{-8}$ m^2/s and $d_w = 2.1 \times 10^{-7}$ m^2/s. However, the value of d_+ taken in the simulations is adjusted in the fitting process. The linear increase of diffusivity with water content reflects, in a phenomenological manner, the change in water-ion interaction within the membrane nanopores as well as the change of membrane morphology and pore structure under water uptake. Because c_w and c_+ are related by Eq. 20 and LEN demands that $J_+ = I/F$, the Eq. 21 and 22 constitute two ordinary differential equations for the membrane potential ϕ and the free water concentration c_w.
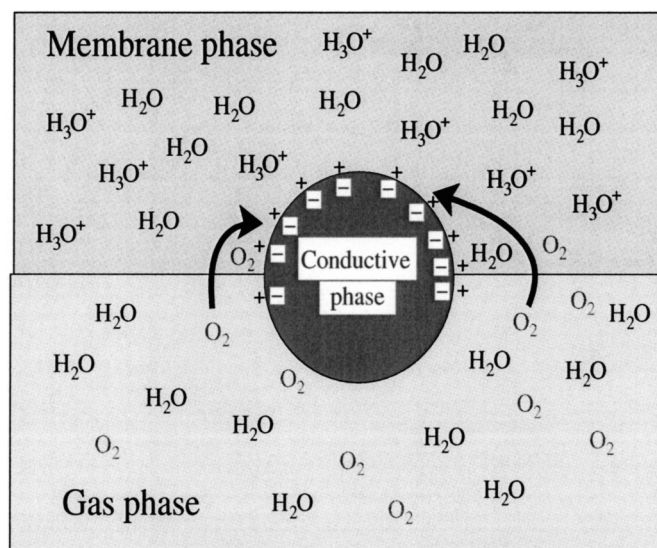
Figure 2. The diffusive path for O_2 to the active catalyst sites. Henry's law is enforced at the membrane/GDL interface.

Interface Conditions

The interface conditions which describe the nonequilibrium exchange of mass between the gas channels and the PEM play a fundamental role in water management. They govern the transport of gases through the GDL, the exchange of water between the membrane and channel, and the generation of current at the catalyst layer.

Electrochemistry.—The electrochemical reaction takes place in the catalyst layer, which is taken to be an interface. The current generated, $I = I(x)$, is related to the overpotential $\eta_c = \eta_c(x)$ in the cathode, by the Butler-Volmer equations

$$I = i_{o,c}\left(\frac{C_o^{cl}}{C_o^{ref}}\right)\left[\exp\left(\frac{\alpha_c F}{\mathcal{R}T}\eta_c\right) - \exp\left(-\frac{(1-\alpha_c)F}{\mathcal{R}T}\eta_c\right)\right] \quad [25]$$

The anode overpotential is neglected as it is significantly smaller than the cathode overpotential in the cases considered herein. With this assumption, the fuel stream's impact on the model is only as a source and sink of water vapor for the anode end of the membrane. The limiting electrochemical reactions are assumed to be first order in oxygen concentration in the cathode.[2] The current production is coupled to the channel flow through the catalyst concentrations of oxygen, C_o^{cl}, which varies with distance x along the channel.

Catalyst/membrane interface.—Active catalyst sites require a stream of protons conducted through the membrane phase, electrons from the conductive phase, and oxygen from the gas phase. We assume these sites are found at the catalyst/membrane interface, with oxygen arriving by diffusion through the liquid and/or bound water of the membrane phase, (Fig. 2). At the boundary of the membrane we impose Henry's law for the absorption of oxygen into the membrane water. The oxygen concentration in the gas phase just outside the membrane, C_o^{m-}, is taken proportional to C_o^{cl}, the oxygen concentration inside the membrane at the catalyst layer

$$C_o^{m-} = \frac{H_o}{RT}C_o^{cl} \quad [26]$$

At 80°C, $RT/H_o \approx 0.15$,[11] which leads to a significant jump in oxygen concentration between the membrane/GDL interface. In the operational FC, the oxygen concentration is influenced by mass transport limitations arising from boundary layers in the channel flow, water pore blockage in the GDL, diffusion losses for O_2

through water to reach the reaction sites, and interspecies diffusive losses. These effects are incorporated into the model via an effective diffusivity D_o^{eff} through the mass transport condition

$$J_o = -\frac{D_o^{eff}}{L_G}(C_{c,1} - C_o^{m-}) \quad [27]$$

For a 1-D model, at steady state, the stoichiometry implies that $J_o = -I/4F$. Combining these two relations yields

$$C_o^{m-} = C_{c,1} - \bar{\delta}I \quad [28]$$

where the fitted parameter $\bar{\delta} = L_G/4FD_o^{eff}$ has been introduced. The membrane has an equilibrium water sorption value, denoted c_w^*, experimentally measured as a function of temperature and water activity a_w (relative humidity, RH) of its environment.[13] At typical PEM FC operating temperatures in the dry (water vapor only) regime

$$c_w^* = 0.043 + 17.81a_w - 39.85a_w^2 + 36a_w^3 \quad [29]$$

which was fit for Nafion 117 at 30°C.[20] There is a discontinuity in c_w^* at the transition to the liquid regime for which the water uptake mechanism is apparently different. For consistency with the dry GDL assumption, the so-called "Schroeder paradox," [21] is disregarded, and the continuous value $c_w^*(a_w = 1) = 14$ is used for a saturated environment.

Several models[3,5-9,11,19] have imposed the condition that the membrane water content, at its boundary, is given by the equilibrium value c_w^*. However, as discussed in the introduction, the time scales associated to the water flux in the membrane dominate the relaxation time, on the order of 100-1000 s,[13,14] required for the membrane to assume its equilibrium hydration state. A key feature of the model presented here is the replacement of an equilibrium assumption with a two-mode water transfer condition.[22] The membrane water contents, c_w^a and c_w^c, at the anode and cathode are capped at a maximum of 14, and while they are under this maximum value, a water transfer mechanism of the form[23]

$$J_w^a/a = -\bar{\gamma}[c_w^a - c_{w,a}^*] \quad [30]$$

$$J_w^c/a = \bar{\gamma}[c_w^c - c_{w,c}^*] \quad [31]$$

is imposed. Here $c_{w,a}^*$ and $c_{w,c}^*$ are the anode and cathode water sorption equilibrium values, based upon the water activities of the corresponding channel. The water transfer coefficient $\bar{\gamma}$, to be determined by the fitting procedure, models mass transport limitations arising from the GDL and the water transfer into and out of the membrane. In the discussion the order of magnitude of this parameter is linked to local water transport through the membrane interface.

The sources of water at the catalyst layers must be taken into account. At the anode, there is a sink, I/F, due to the osmotic drag of water with the current. At the cathode catalyst layer there is a source, $J_+ = 3I/2F$, due to water produced by the reaction and brought by the osmotic drag. Conservation of mass implies that the difference in fluxes across the catalyst layers equal to sources

$$\text{anode} \quad J_w - J_w^a = -\frac{I}{F} \quad [32]$$

$$\text{cathode} \quad J_w^c - J_w = \frac{3I}{2F} \quad [33]$$

In the underhydrated case, the mass transfer conditions, Eq. 30, 31, may be written as

$$\text{anode} \quad \left(J_w + \frac{I}{F}\right)\bigg/ a = -\bar{\gamma}[c_w^a - c_{w,a}^*] \quad [34]$$

$$\text{cathode} \left(J_w + \frac{3I}{2F}\right) \bigg/ a = \bar{\gamma}[c_w^c - c_{w,c}^*] \qquad [35]$$

The membrane water content typically rises with distance from the air stream inlet until the cathode membrane water content reaches the maximum value 14. In this fully-hydrated case the interface condition, Eq. 31, is replaced with

$$c_w^a = 14 \qquad [36]$$

and the membrane water flux, J_w, and c_w^a, are calculated from Eq. 30 and 22. The balance of the water flux, J_w^c, is forced out into the cathode stream according to Eq. 33. The under-hydrated mechanism, Eq. 30, 31, models water transfer by a phase-change-like process, while the fully hydrated mechanism represents forces arising from membrane swelling which expel liquid water from the membrane.

Model Reduction, Experimental Details, and Fitting

The membrane model consisted of a family of ordinary differential equations (ODEs) for the y variation of water concentration and potential, coupled to each other through the channel flow. In this section, the membrane portion of the model is explicitly reduced to algebraic equations for the current $I(x)$, and the fluxes $J_w^a(x)$ and $J_w^c(x)$ of water between the membrane and the anode and cathode channels, respectively.

The external potential U, assumed to be independent of x (assumption 5), satisfies the following Kirchoff-type relation

$$U = E_o - \eta_c - \phi_m \qquad [37]$$

where the anode overpotential and all losses associated to the GDL or graphite plates are neglected. The membrane losses, ϕ_m, will depend upon the membrane water content, and implicitly through the channel water content and local current $I(x)$. The open circuit voltage, E_o, is a prescribed constant.

From Eq. 25 the overpotential, η_c, is an explicit function of the current density and the oxygen concentration in the membrane, which is approximated by its Tafel form

$$\eta_c \simeq \frac{\mathcal{R}T}{\alpha_c F} \ln\left(\frac{IC_o^{ref}}{i_{o,c} C_o^{cl}}\right) \qquad [38]$$

at high currents. In turn, C_o^{cl} can be expressed via Henry's law, Eq. 26, and 28 in terms of the current density and the known channel concentration as

$$C_o^{cl} = \frac{\mathcal{R}T}{H_o}(C_{c,1} - \bar{\delta}I) \qquad [39]$$

Denoting the membrane water content at the anode and cathode by c_w^a and c_w^c, respectively, the water flux Eq. 22 is integrated from anode to cathode to obtain

$$J_w = a d_w e^{-2436/T} \frac{(c_w^a)^2 - (c_w^c)^2}{2L_m} \qquad [40]$$

where the linear dependence of diffusivity on water concentration, Eq. 24, is reflected in the quadratic dependence of flux, J_w, on membrane boundary water concentrations. The relations Eq. 34, 35, and 40, constitute three equations for the unknowns c_w^a, c_w^c, and J_w which have the explicit solution

$$c_w^c = \frac{1}{2}(\xi_+ + \xi_-) \qquad [41]$$

$$c_w^a = \frac{1}{2}(\xi_+ - \xi_-) \qquad [42]$$

where

$$\xi_+ = c_{w,c}^* + c_{w,a}^* + \frac{I}{2\bar{\gamma}aF} \qquad [43]$$

$$\xi_- = \frac{c_{w,c}^* - c_{w,a}^* + \dfrac{5I}{2\bar{\gamma}aF}}{1 + \dfrac{d_w e^{-2436/T}\xi_+}{L_m \bar{\gamma}}} \qquad [44]$$

The water concentrations c_w^a and c_w^c depend upon channel water activities through the water sorption equilibria and upon current I. In the limit of an infinite water transfer coefficient, $\bar{\gamma} \to \infty$, the equilibrium sorption values, $c_w^c = c_{w,c}^*$ and $c_w^a = c_{w,a}^*$ are recovered, while decreasing $\bar{\gamma}$ increases the average membrane water content $(c_w^a + c_w^c)/2 = \xi_+/2$ and, therefore, its conductivity. Also, increasing current increases the difference between c_w^c and c_w^a, which is consistent with the electro-osmotic drag and water production at the cathode.

Having determined the membrane water concentration, c_w, the proton concentration is known from Eq. 20, and the membrane potential losses, ϕ_m, are determined by integrating Eq. 21 across the membrane

$$\phi_m(I) = -\int_0^{L_m} \phi_y \, dy \qquad [45]$$

$$= \frac{\mathcal{R}T}{F} \int_0^{L_m} \frac{J_+/a + D_+(c_w)c_{+,y}}{D_+(c_w)c_+} \, dy \qquad [46]$$

$$= \left(\frac{\mathcal{R}T}{aF^2} \int_0^{L_m} \frac{dy}{D_+(c_w)c_+}\right)I + \frac{\mathcal{R}T}{F}\ln\left(\frac{c_+^a}{c_+^c}\right) \qquad [47]$$

where the equality $J_+ = I/F$ was used. The potential-current relation Eq. 47 suggests the definition of an effective membrane conductivity

$$\sigma = \left(\frac{\mathcal{R}T}{aF^2}\int_0^{L_m}\frac{dy}{D_+(c_w)c_+}\right)^{-1} \qquad [48]$$

which depends implicitly upon the current, $\sigma = \sigma[I(x)]$, through the water content. The concentration polarization, the second term on the right-hand side of Eq. 47, arises from the variation of the hydronium concentration from the anode to the cathode. For typical FC operating conditions, this term takes values on the order of 10 mV, which is a small but not negligible contribution to the ohmic losses of the membrane.

The substitution of Eq. 38 and 47 into Eq. 37, using Eq. 39 and Eq. 48, yields the voltage balance equation

$$U = E_o - \frac{\mathcal{R}T}{\alpha_c F}\ln\left(\frac{C_o^{ref}H_o}{i_{o,c}\mathcal{R}T}\frac{I}{(C_{c,1} - \bar{\delta}I)}\right) - \left[I/\sigma + \frac{\mathcal{R}T}{F}\ln\left(\frac{c_+^a}{c_+^c}\right)\right] \qquad [49]$$

This is solved for $I = I(x)$ in terms of the external voltage U at every x for known channel concentrations through an implicit solve.

Experimental details.—The experimental results were obtained with a custom built current mapping hardware using a single Ballard Mk9 MEA and a subcell approach as described earlier,[24] although the MEA itself was not sectioned. Nafion 112 membrane was used for MEA manufacture. Along the direction of the gas flow, the cathode flow field and cathode current collection plates were divided into 16 electrically insulated sections, allowing the independent control of the load current through each section by 16 load banks. Polarization curves were obtained under constant fuel- and oxidant stoichiometry with respect to the total cell current. For all measure-

ments, the cell voltages of all 16 sections were kept identical (iso-potential conditions) in order to minimize errors due to crosscurrents between different sections. The test cell was operated on a custom designed test station allowing accurate control and monitoring of all operating parameters. Cell temperatures are given by the coolant inlet and outlet temperatures, respectively. Water balance measurements were carried out using RH sensors for reactant inlet and outlet streams. Outlet humidities were reduced to less than 100% by addition of a sufficient amount of dry gas to anode and cathode exit gas streams. The experimental data is collected for runs with air, helox, and pure O_2 as the oxidant. The Helox (helium-oxygen) gas mixture contained helium in the same percentage as the nitrogen in air.

Fitted parameters and fitting procedure.—Four fitted parameters were incorporated into the model: cathode exchange current density $i_{o,c}$, oxygen mass transfer coefficient $\bar{\delta}$, the water transfer coefficient $\bar{\gamma}$, and an average membrane conductivity $\bar{\sigma}$. These quantities depend sensitively on the micro-and nano-level structure of the MEA and catalyst layer, and on the possible presence of liquid water in the channels and GDL.

Each data family consisted of n runs of the same oxidant composition (air/helox/pure O_2). Each run recorded current density at 16 locations down the channel of a unit cell, inlet and outlet temperature, pressure, and mixture data and overall cell voltage. The inlet relative humidity and stoichiometry and the total cell current were prescribed. For the fitting procedure the channel model was run on a 16-point grid using the local current density from the data to calculate the local channel oxygen concentration at the 16 points. In addition to the assumptions in the main model, for the data fitting, the membrane resistance was assumed to be independent of temperature, while the dependence on humidity levels was minimized by fitting at humid operating conditions for which membrane water content was uniformly high.

For each data family, $16n$ conditions for current density $I_{k,m}$, oxygen concentration $C_{k,m}$, and temperature $T_{k,m}$ were obtained. Here $m = 1, \ldots, n$ denotes the run number and $k = 1, \ldots, 16$ the position down the channel. There are also n conditions for the cell voltage U_m. In terms of these parameters the local balance equation takes the form

$$res_{k,m} = E_o - U_m - I_{k,m}/\bar{\sigma} - \frac{RT_{k,m}}{F\alpha_c} \ln\left(\frac{I_{k,m}}{i_{o,c}} \frac{c_{o,ref}}{C_{k,m} - \delta I_{k,m}}\right)$$

$$[50]$$

where the local residual $res_{k,m}$ measures the amount by which the voltage balance equations fails to be satisfied. The reduced reference oxygen concentration, $c_{o,ref} = C_o^{ref} H_o/\mathcal{R}T$, has Henry's law built in, where $C_o^{ref} = 40.9$ mol/m^3 corresponds to pure oxygen at 1 atm. The average membrane conductivity $\bar{\sigma}$ is fitted as a constant along the length of the channel. This value was used in the main code by adjusting the constant d_+, defined in Eq. 23, so that the membrane conductivity σ defined by Eq. 48 satisfied $\sigma = \bar{\sigma}$ at full hydration and $T = 70°C$. To simplify the calculation, the concentration polarization was neglected in the fitting procedure.

Nonlinear optimization (Nelder-Mede) was used to minimize the sum (RES), of the squares of the $16n$ residuals

$$RES = \sum_{m=1}^{n} \sum_{k=1}^{16} (res_{k,m})^2 \qquad [51]$$

which provided the values for the exchange current, $\bar{\delta}$ and the membrane resistance.

Results and Discussion

Counter-flow: fitting results.—There are three data families, based upon oxidant type. The values from the air and helox fittings are
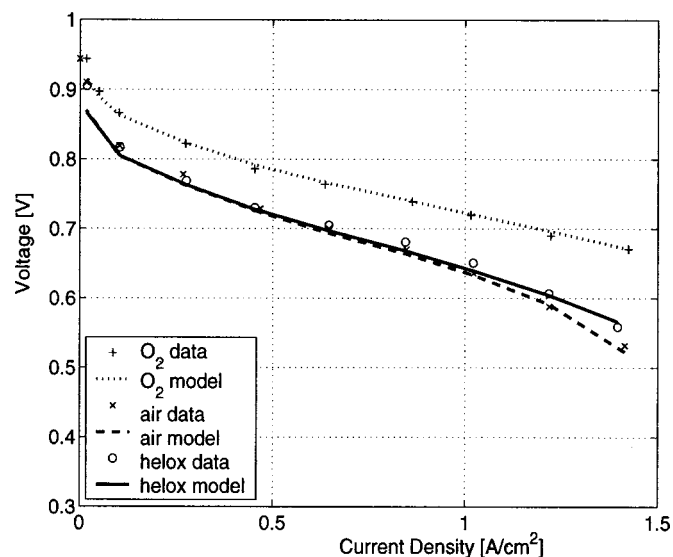

Figure 3. Polarization curves for oxygen, air, and helox as oxidant gas: comparison of data and model predictions for counter-flow configuration. Operating conditions: anode/cathode pressure 2.2/2.0 barg, $T_{in} = 70°C$, $T_{out} = 80°C$, H2/oxidant stoichiometry: 1.2/1.8, anode/cathode dew points; 66/66°C. Fit parameters for air and oxygen: $i_{o,c} = 42.67$ mA/cm^2, $\bar{\delta} = 0.899 \times 10^{-3}$ mol/Am, $\bar{\sigma}^{-1} = 93.73$ mΩ cm^2. Fit parameters for helox: $i_{o,c} = 42.93$ mA/cm^2, $\bar{\delta} = 0.794 \times 10^{-3}$ mol/Am, $\bar{\sigma}^{-1} = 88.5$ mΩ cm^2. The water transfer coefficient $\bar{\gamma} = 5.7 \times 10^{-6}$ m/s for all cases.

$$\text{Air} \quad i_{o,c} = 4.26 \times 10^2 \text{ A/m}^2 \qquad [52]$$

$$\bar{\delta} = 0.899 \times 10^{-3} \text{ s mol m}^{-1} \text{ C}^{-1} \qquad [53]$$

$$\bar{\sigma}^{-1} = 0.0937\Omega \text{ cm}^2 \qquad [54]$$

and

$$\text{helox} \quad i_{o,c} = 4.29 \times 10^2 \text{ A/m}^2 \qquad [55]$$

$$\bar{\delta} = 0.794 \times 10^{-3} \text{ s mol m}^{-1} \text{ C}^{-1} \qquad [56]$$

$$\bar{\sigma}^{-1} = 0.0885 \ \Omega \text{ cm}^2 \qquad [57]$$

Twelve sets of data were used for the air oxidant fit, and four for helox. The average residuals for both fits were less than 3 mV. The oxygen data set was small, while the computational results showed little variation in oxygen or current along the channel. These traits exaggerated the error in the fitting parameters, to compensate, the air values are taken for the fitted parameters in the O_2 polarization curve calculations. The fitted value of the exchange current $i_{o,c}$ is within 1% for both oxidant types. The membrane conductivity was not expected to vary between oxidant types, and the observed difference was small enough that it can be ascribed to data variability in the small set of helox data.

In further calculations of the main model for the air data, the exchange current was set at $i_{o,c} = 4.26 \times 10^2$ A/m^2. The fitted parameter $\bar{\delta}$ for air corresponds to an effective oxygen diffusivity of $D_o^{eff} = L_G/4F\delta = 7.2 \times 10^{-7}$ m^2/s for the given oxidant type. The average resistivity of 0.09373 Ω cm^2 compares to literature values of 0.0614 Ω cm^2 for Nafion 112[13] at full humidification. The implementation of $\bar{\sigma}$ in the code results in setting $d_+ = 1.42 \times 10^{-8}$ m^2/s, about 10% smaller than some literature values, but permits a fitting of the polarization curves in Fig. 3. The fitted values of D_o^{eff} are an order of magnitude lower than the binary diffusivity of O_2 in N_2, 1.04×10^{-5} m^2/s, and show little change when the N_2 in air is replaced with helium in the helox runs, even though the binary
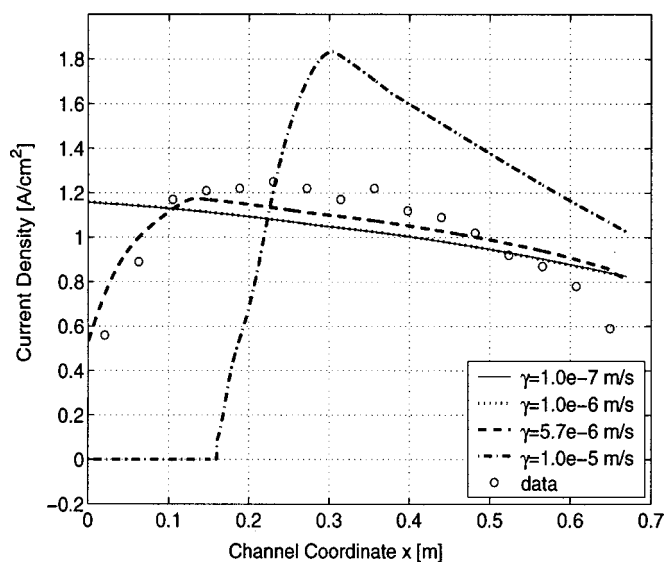
Figure 4. Current distribution for the dry case (see Table III) and fuel counter-flow configuration. Comparison between data and model prediction for 4 different values of water transfer coefficient $\bar{\gamma}$. Note the curves for $\bar{\gamma} = 10^{-6}$ m/s and $\bar{\gamma} = 10^{-7}$ m/s are indistinguishable (limiting case $\bar{\gamma} \rightarrow 0$). For $\bar{\gamma} > 10^{-5}$ m/s the predicted current density drops to 0 at the dry cathode inlet. Other fit parameters are as for air in Fig. 3.
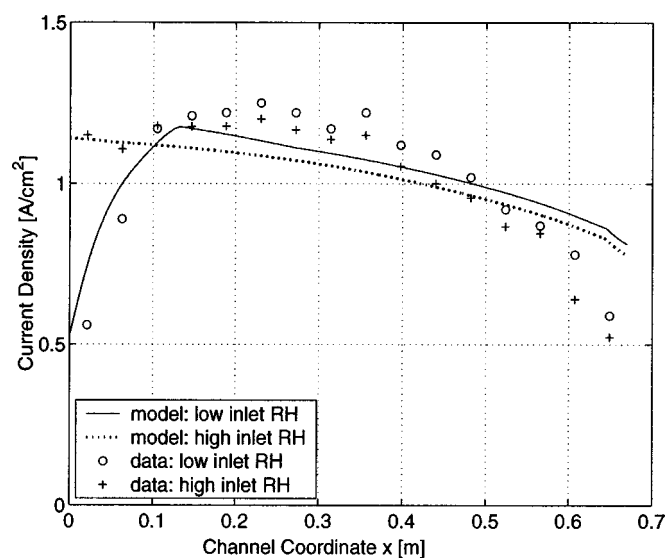

Figure 5. Current distribution along the flow direction for dry and moderate air humidification and fuel counter-flow configuration (see Fig. 1): comparison of data and model calculations for an overall current density of 1A/cm². Operating conditions are given in Table III. The water transfer coefficient $\bar{\gamma} = 5.7 \times 10^{-6}$ m/s.

diffusivity of oxygen differs by a factor of three.[25] The reduced diffusivity cannot be attributed to Henry's law, which is accounted for in the model. This evidence supports the conjecture that the active catalytic sites are predominantly located within the membrane and that diffusion of O_2 dissolved into the membrane H_2O over the short path from GDL to embedded catalyst site plays a significant role in mass transport limitations (see Fig. 2). This path length can be estimated by replacing D_o^{eff} with the diffusivity of oxygen in water, $D_o^m = 10^{-10}$ m²/s, and solving for the diffusive length for oxygen, $L_m = 4F\bar{\delta}D_o^m \approx 35$ nm, which is one order of magnitude greater than a typical platinum particle diameter.

The water transfer coefficient, $\bar{\gamma}$, was determined in a one-time fashion from the run with the lowest cathode inlet RH by fitting the along-the-channel current data to that produced by the full model, see Fig. 4. This trial-and-error method gave a value of $\bar{\gamma} = 0.57 \times 10^{-5}$ m/s, which was used in all other computations.

The order of magnitude of the water transfer coefficient $\bar{\gamma}$ can be independently estimated by relating it to observed membrane equilibrium time scales available in the literature.[13,20] For an isolated membrane occupying the domain $0 < y < L_m$ with initially uniform water concentration $c_w(y,0) = c_{w0}$, the simplest model for the water transport within the membrane is a linear diffusion model

$$(c_w)_t - D \frac{\partial^2 c_w}{\partial y^2} = 0 \qquad [58]$$

For a membrane placed in an ambient surrounding whose RH induces an equilibrium water concentration c_w^*, with the boundary condition for the flux $J_w = -D(c_w)_y$ at the end point $y = 0$

$$-D(c_w)_y = \bar{\gamma}(c_w - c_w^*) \qquad [59]$$

while at the midpoint, $y = L_m/2$, a symmetry condition is imposed

$$(c_w)_y = 0 \qquad [60]$$

Solutions take the form

$$c_w(y,t) = c_w^* + \sum_{k=1}^{\infty} f_k(y)\exp(-\lambda_k t) \qquad [61]$$

The water concentration, c_w, will tend to the equilibrium value c_w^* at a rate $e^{-\lambda_0 t}$, where the time scale of relaxation λ_0^{-1} is related to $\bar{\gamma}$

$$\tan(\sqrt{\lambda_0/D}\ L_m/2) = \frac{\bar{\gamma}}{\sqrt{\lambda_0 D}} \qquad [62]$$

In the thin membrane regime, $\sqrt{\lambda_0/D}\ L_m/2 \ll 1$, the diffusivity is so large, as measured against membrane thickness and hydration time scale, that the hydration time is dominated by the water transfer coefficient $\bar{\gamma}$. Within this regime, the approximation $\tan w = w + O(w^3)$ yields $\bar{\gamma} \simeq \lambda_0 L_m/2$, and the diffusivity influences $\bar{\gamma}$ only at higher order. From the data in Ref. 13, for a membrane of width $L_m = 250$ μm, the time scale for hydration is $\lambda_0^{-1} \simeq 100$ s, while the membrane diffusivity is $D \simeq 10^{-9}$ m²/s.[9] These yield $\sqrt{\lambda_0/D}\ L_m/2 \approx .5$ which is at the limit of the thin membrane reduction and an estimate for the water transfer coefficient $\bar{\gamma} \simeq \lambda_0 L_m/2 \simeq 10^{-5}$ m/s. This estimate, based entirely upon water uptake considerations for the membrane is close to the fitted value. An estimate developed from diffusive losses in the GDL, along the lines of Eq. 27, would suggest $\bar{\gamma} \approx D_{H_2O}/L_G = 8 \times 10^{-6}$ m²/s/250 μm $= 3 \times 10^{-2}$ m/s, which is almost four orders of magnitude above the fitted value. These simple scaling arguments suggest that water vapor transfer from the membrane to the channel is dominated by processes occurring at the boundary of the membrane and not in the gas diffusion layer.

In Fig. 5-8, two different cases of cathode inlet relative humidities are considered. The operation conditions are given in Table III. An important feature of the along-the-channel current density is the "inlet blip" experienced for dry cathode inlets. This drop-off in current production occurs for counter-flowing configurations when the cathode inlet RH is less than 50%. In Fig. 5, the model captures the inlet-blip for the low inlet RH run, as well as its absence in the high-inlet RH run. The data shows a plateau of current production from $x = 0.15\text{-}0.3$ m, followed by a drop-off in current production
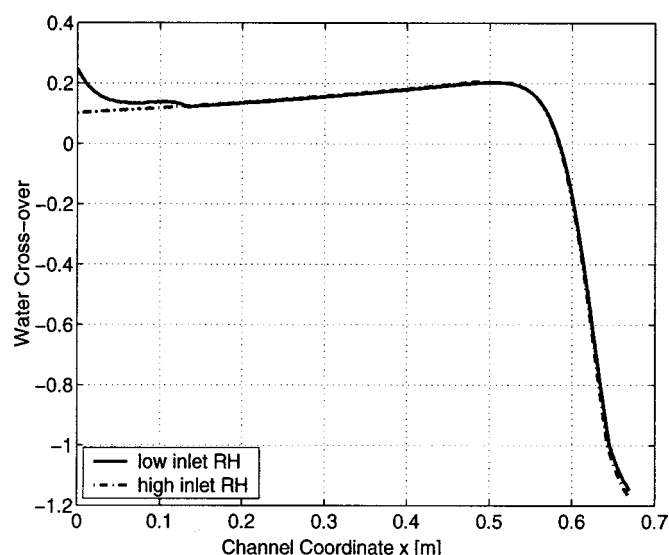
Figure 6. Calculated water transfer α for dry and moderate air humidification (see Table III) and fuel counter-flow configuration (Fig. 1). Whereas the majority of the channel is dominated by the anode inlet conditions which are identical for both cases, the lower cathode humidification leads to a higher water transfer at the left side of the channel.

towards the cathode outlet. The model captures the general trend of lower current production toward the cathode outlet, but does not capture the plateau, and underestimates the slope of the drop-off. This can be attributed to two aspects of the model, the capping of membrane water content at 14, which precludes a highly conductive moist membrane in the midstream, and the absence of liquid water in the GDL, which likely increases toward the cathode outlet, impeding O_2 flow to the membrane. Moreover, at constant total current, an elevated local current in the midchannel range will consume
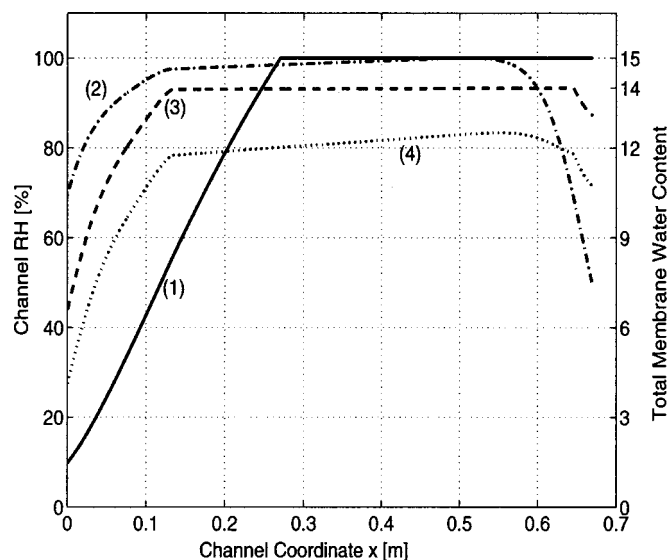

Figure 7. Calculated water concentration profiles in the gas streams and on both sides of the membrane for the dry case (see Table III) and the fuel counter-flow configuration. (1) Relative humidity (RH) along the cathode flow, (2) RH along the anode flow, (3) and (4), membrane interface water contents at the cathode and anode sides, respectively. The cathode flow stays undersaturated for about 30% of the channel length and humidifies the anode flow (see Fig. 6). The water transfer coefficient $\bar{\gamma} = 5.7 \times 10^{-6}$ m/s.
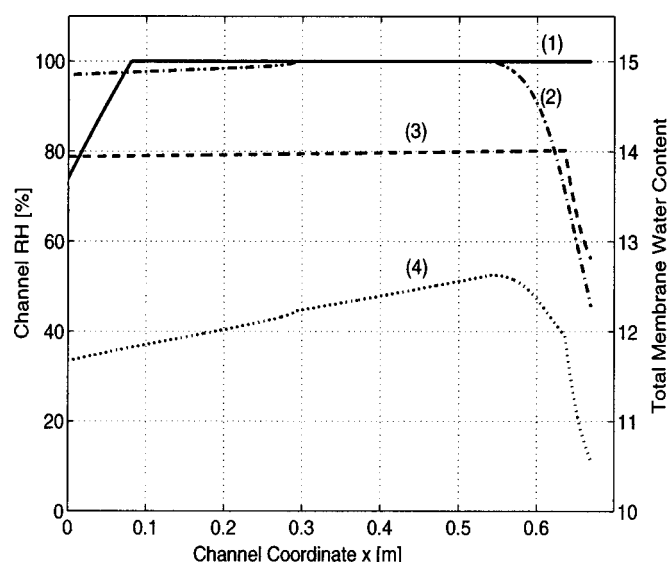

Figure 8. Calculated water concentration profiles in the gas streams and on both sides of the membrane for the moderate case (see Table III) and fuel counter-flow configuration. (1) Relative humidity (RH) along the cathode flow, (2) RH along the anode flow, (3) and (4), membrane interface water contents at the cathode and anode sides, respectively. The cathode flow saturates after less than 10% of the channel length. The water transfer coefficient $\bar{\gamma} = 5.7 \times 10^{-6}$ m/s.

more O_2, starving the outlet range and enhancing the drop-off in current. Capturing the influence of two-phase flow in the GDL is outside the scope of this model.

The water transfer (see Fig. 6) is chiefly from anode to cathode, except for a short range near the anode inlet. The total water transfer was similar for both the high and low cathode inlet RH cases. However, the water transfer was substantially higher at the cathode inlet for the low RH case. In both cases, the anode and cathode RH drop at the cathode inlet, see Fig. 7,8. The drop in anode RH was due to the water transfer pulling water into the cathode air stream, and was enhanced by the diminished capacity of the depleted anode stream to carry water vapor. The cathode streams remained fully saturated after their initial saturation, which occurred at roughly $x = 0.1$ m for the moderate case and $x = 0.3$ m in the dry case. In the low inlet RH case, the membrane water content reached its maximum value, 14, on the cathode side significantly before the cathode channel saturated. That is a significant feature of the model: controlling water transport from membrane to channel reduces the sensitivity to inlet RH. The anode membrane water content remained below the saturated value for the whole channel length in both cases, reaching its maximum value just downstream from the anode inlet. The cathode membrane water content dropped from the fully hydrated value at the anode inlet due to the large negative water transfer which dries the cathode side of the membrane while hydrating the anode membrane and anode channel stream (note: anode flow is right-to-left in Fig. 8).

The flux of water carried along-the-channel in liquid form is given by Eq. 13 and is presented in Fig. 9 for both the high and low cathode inlet RHs. The liquid water fluxes were zero until the cathode channel saturated, and then increased until just before the anode inlet, where the back diffusion pulled water out of the cathode stream. For the low inlet RH case, the vapor flux was roughly twice the liquid flux at the cathode outlet, while for the high inlet RH case the liquid flux was comparable to the vapor flux at the outlet. The liquid water channel area fraction, A_L, is defined as the ratio of the liquid water volume fraction to the channel cross section area, A_c.

Table III. Operating conditions for counter-flowing configuration with dry (low inlet RH) and moderate (high inlet RH) cases at I_{avg} = 1 A/cm^2. Fuel: H$_2$, oxidant: air. The coflowing configuration is a moderate inlet RH at I_{avg} = 1.0 A/cm^2.

	Dry case counter-flow	Moderate case counter-flow	Moderate case co-flow
U_{exp} (V)	0.637	0.646	0.646
U_{mod} (V)	0.627	0.633	0.631
Computed α_T (%)	7.1	6.5	5.4
P_a (atm)	2.2	2.2	2.2
P_c (atm)	2.0	2.0	2.0
S_a	1.2	1.2	1.2
S_c	1.8	1.8	1.8
$T_{a,dew}$ (°C)	63	63	63
$T_{c,dew}$ (°C)	23	63	63
T (cathode inlet→outlet) (°C)	70→80	70→80	70→80

a_w	Water activity (dimensionless)
c_b	Bound proton concentration of membrane, mol/m^3
c_w	Free water concentration of membrane, mol/m^3
c_w^a	Membrane water content at anode side, mol/m^3
c_w^c	Membrane water content at cathode, mol/m^3
c_+	Hydronium concentration of membrane, mol/m^3
c_+^c	Hydronium concentration at cathode side, mol/m^3
c_+^a	Hydronium concentration at anode side, mol/m^3
c_T	Total water concentration of membrane, $c = c_w + c_+$, in mol/m^3
c_w^*	Water sorption equilibrium, mol/m^3
$c_{w,a}^*$	Water sorption equilibrium at anode, mol/m^3
$c_{w,c}^*$	Water sorption equilibrium at cathode, mol/m^3
C_a	Vector $(C_{a,1}, C_{a,2})$ of C_a values
$C_{a,1}$	Anode channel concentration of H$_2$, mol/m^3
$C_{a,2}$	Anode channel concentration of vapor, mole/m^3
C_c	Vector $(C_{c,1}C_{c,2}, C_{c,3})$ of C_c values
$C_{c,1}$	Cathode channel concentration of O$_2$, mol/m^3
$C_{c,2}$	Cathode channel concentration of vapor, mol/m^3
$C_{c,3}$	Cathode channel concentration of N$_2$, mol/m^3
C_o^{cl}	Oxygen concentration in GDL at cathode catalyst layer, mol/m^3
C_o^{m-}	Oxygen concentration in membrane at cathode catalyst layer, mol/m^3
D_o^{eff}	Oxygen effective diffusion coefficient m^2/s
I	Current density in A/cm^2
I_{avg}	Average current density A/cm^2
J_+	Hydronium flux mol m^{-2} s^{-1}
J_o	Oxygen flux mol m^{-2} s^{-1}
J_w	Free water flux mol m^{-2} s^{-1}
J_w^T	Total water flux, $J_w^T = J_w + J_+$, mol m^{-2} s^{-1}
J_w^c	Water flux in cathode GDL mol m^{-2} s^{-1}
J_w^a	Water flux in anode GDL mol m^{-2} s^{-1}
P	Channel pressure, Pa
P_a	Anode channel pressure, Pa
P_c	Cathode channel pressure, Pa
P_{sat}	Saturation pressure, Pa
P^w, P_2	Water partial pressure in channel, Pa
p_{cap}	Capillary pressure in membrane, Pa
Q_a	Vector $(Q_{a,1}, Q_{a,2})$ of Q_a values
$Q_{a,1}$	Anode channel flux of H$_2$ mol/s
$Q_{a,2}$	Anode channel flux of H$_2$O mol/s
Q_c	Vector $(Q_{c,1}, Q_{c,2}Q_{c,3})$ values
$Q_{c,1}$	Cathode channel flux of O$_2$ mol/s
$Q_{c,2}$	Cathode channel flux of H$_2$O mol/s
$Q_{c,3}$	Cathode channel flux of N$_2$ mol/s

This may be calculated from the liquid flux Eq. 13 under the assumption that the liquid travels as suspended droplets with the gas velocity

$$A_L(x) = \frac{Q_{c,l}}{C_l V_c A_c} \qquad [63]$$

Under this assumption, A_L, as depicted in Fig. 9, takes values on the order of 10^{-4}. A rough estimate of the ability of the fuel stream to hydrate the membrane anode can be obtained from examining the ratio of the anode stream water flux to the osmotic drag. For a FC operating at anode inlet flow of H$_2$/H$_2$O, pressure $P_{a,in}$, temperature $T_{a,in}$, stoichiometry S_a, and partial water pressure $P_{a,in}^w$, assum-
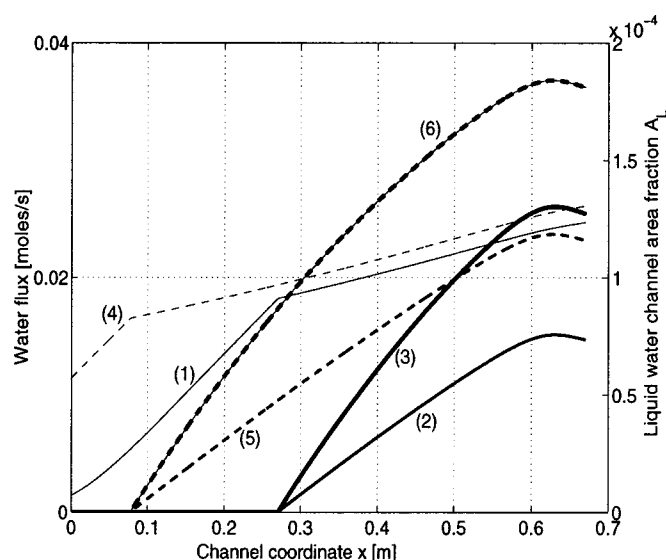
Figure 9. Calculated liquid and vapor fluxes in the cathode flow channel for the dry and moderate cases (see Table III) and fuel counter-flow configuration. (1) Water vapor and (2) liquid water fluxes for the dry case, (4) water vapor and (5) liquid water fluxes for the moderate case. The channel cross section occupied by liquid water, A_L is given in (3) the dry case and in (6) the moderate case. The liquid water flux is zero until the channel saturates, at about 10% of channel length for moderate case and 40% for dry case.

Figure 10. Current distributions for different cathode flow air humidification levels under fuel counter-flow configuration, comparison between data and model prediction. All fit parameters as for air in Fig. 3. Except for dew point, the operating conditions are as given in Table III.

ing undersaturated conditions, the ratio of the water flux, $Q_{a,2}(L_c)$, to the hydrogen flux, $Q_{a,1}(L_c)$, at the anode channel inlet is proportional to the corresponding pressures

$$\frac{Q_{a,2}(L_c)}{Q_{a,1}(L_c)} = \frac{P_{a,in}^w}{P_{a,in} - P_{a,in}^w} \qquad [64]$$

If the cell is producing a total current I_T, then

$$Q_{a,1}(L_c) = \frac{S_a I_T}{2F} \qquad [65]$$

On the other hand, the amount of water carried from anode to cathode by osmotic drag is NI_T/F. The ratio

$$A_w = \frac{Q_{a,2}(L)}{NI_T/F} \qquad [66]$$

describes the balance between water carried by the anode stream and water required to satisfy electro-osmotic drag. For the inlet conditions as in the moderate case of Table III, and assuming $N = 1$, one finds that $A_w = 0.06 \ll 1$. The vast majority of water required at the anode must come from the cathode by back diffusion.

The sensitivity of the current profile to the water transport coefficient $\bar{\gamma}$ is displayed in Fig. 4 which shows low cathode inlet RH data. For $\bar{\gamma}$ varying over one order of magnitude, the computed current profiles run from the case of complete insensitivity to inlet RH for $\bar{\gamma} \leqslant 1.0 \times 10^{-6}$ m/s to a "dry cell" state at $\bar{\gamma} \geqslant 1.0 \times 10^{-5}$ m/s in which the segment of membrane adjacent to the dry inlet exhibits no current and very low water content. In Fig. 10 the computed along-the-channel current profiles capture the inlet blips for runs with dew points of 0°C, 23, 33, and 43°C. This is obtained with the same fit parameters, including $\bar{\gamma}$, despite its sensitivity. Again, the midchannel current plateaus are not captured by the model.

There is no along-the-channel experimental data on channel RH or membrane water content. However for cathode inlet RH over
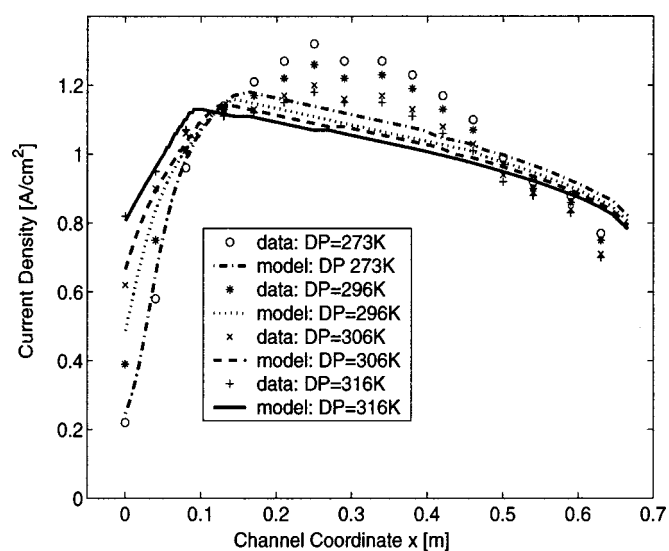
50%, the experimental data shows little dependence on inlet RH, suggesting a fully saturated membrane, in agreement with the computational results (see curves 3 and 4 of Fig. 8).

The dependence of the overall cell voltage on the cathode stoichiometry, see Fig. 11, is well described by the model at normal operational conditions. At the low cathode stoichiometry $S_c = 1.1$, the FC performance is irregular and highly sensitive to inlet conditions and buildup of liquid water. The model predicts cell failure at this low inlet stoichiometry, while the data suggests this phenomena occurs at a slightly low cathode stoichiometry.

The predictive power of the model with the four fit parameters is indicated in Fig. 12, a scatter plot of 37 different counter-flow air runs. The horizontal axis shows experimentally measured total water transfer plotted against the computed values for anode inlet due points ranging from −5 to 75°C and cathode inlet dew points from
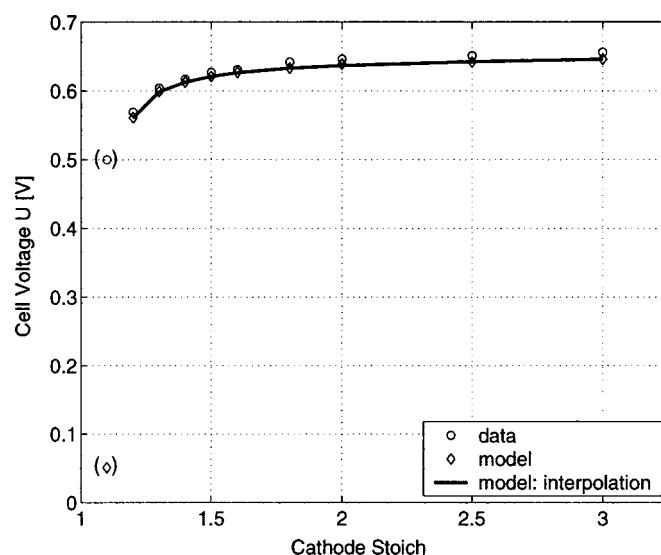

Figure 11. Air stoichiometric sensitivity of cell voltage at 1 A/cm². For S_c < 1.1 cell performance is highly sensitive, the model predicts cell failure slightly higher stoich than data. The other operating conditions are as given in the moderate case of Table III.
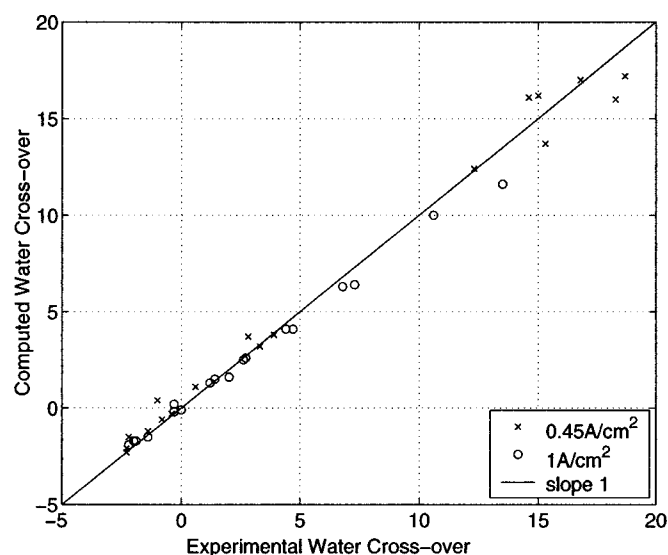
Figure 12. Total water transfer, in percent, at 0.45 A/cm² and 1 A/cm² as a function of anode and cathode humidification for counter-flow configuration. Operating conditions. (Diamonds) 0.45 A/cm²: anode/cathode pressure 2.5/2.5 bar gauge (bar), $T_{in} = 70°C$ $T_{out} = 72°C$, H_2/oxidant stoichiometry 1.2/1.8, anode/cathode dew point range: −5 to 75°C/−24 to 77°C. (Circles) 1.0 A/cm²: anode/cathode pressure 2.0/2.0 bar, $T_{in} = 70°C$ $T_{out} = 80°C$, H_2/oxidant stoichiometry 1.2/1.8, anode/cathode dew point range: −5 to 75°C/−24 to 77°C.

Figure 14. Calculated water transfer α for moderate RH counter-flow and coflow configurations (Table III) at $I_{avg} = 1$ A/cm². A significant anode water removal effect, negative α, is seen for coflow operation at cathode inlet. For counter-flow operation a strong anode water removal effect serves to humidify the anode inlet.

−24 to 77°C. The distance of the data points from the diagonal line is a measure of error. The computed values agree with the experimental ones to within 5% over this tremendous range of operating conditions, using only four fit parameters obtained from an entirely different set of operating data.

Comparison to co-flow.—This section compares model results and data for a coflowing fuel configuration with those from a counter-flowing configuration at similar operating conditions, see Fig. 13-15. The operating conditions for the coflow are given by the third column of Table III. Note that while the dew points at the fuel
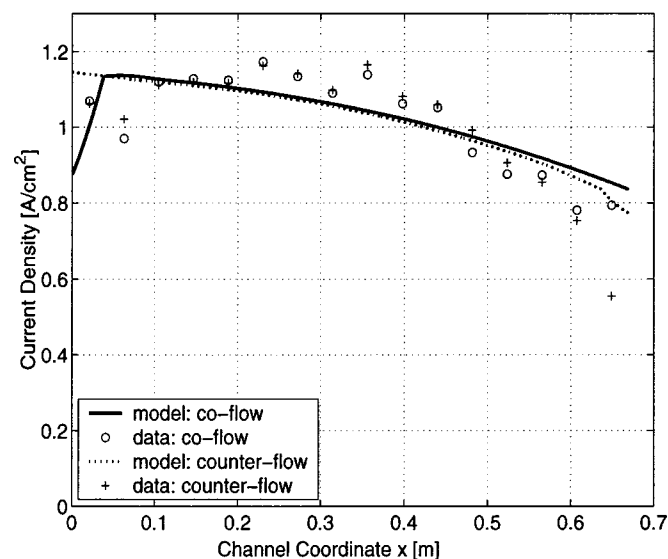
inlet was 63°C for both configurations, the counter-flowing fuel inlet was at the 80°C end of the cell, so the corresponding relative humidity was lower. The salient difference between the two operational configurations is seen in the distribution of water in the membrane along the channel. This is reflected in the along-the-channel current density profiles, Fig. 13, for which the model shows a current blip for the coflow case even at high inlet RH. No current blip was seen for any of the counter-flow runs with high inlet humidity. While the inlet blip is not conclusively supported by the current profile data set, Fig. 15 shows that both the anode channel RH and the anode membrane water content at the inlet are appreciably lower

Figure 13. Current distributions for fuel co- and counter-flow configurations at 1 A/cm², the operating conditions are from the moderate and coflow columns of Table III. The only significant differences in the model calculations appear at the air inlet. The water transfer coefficient $\bar{\gamma} = 5.7 \times 10^{-6}$ m/s.
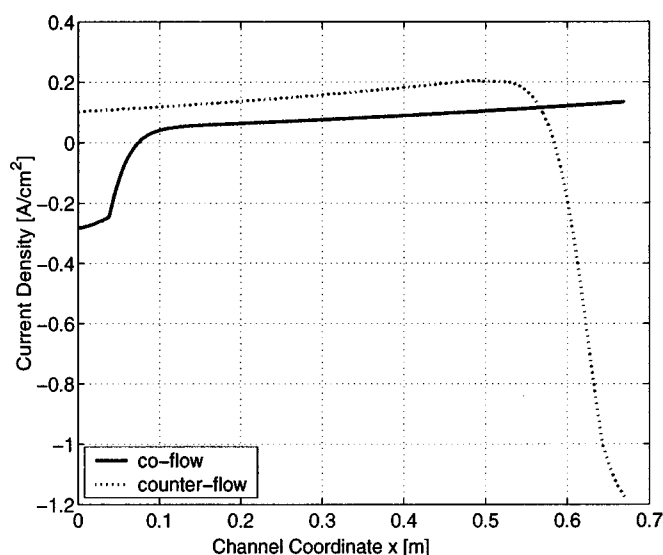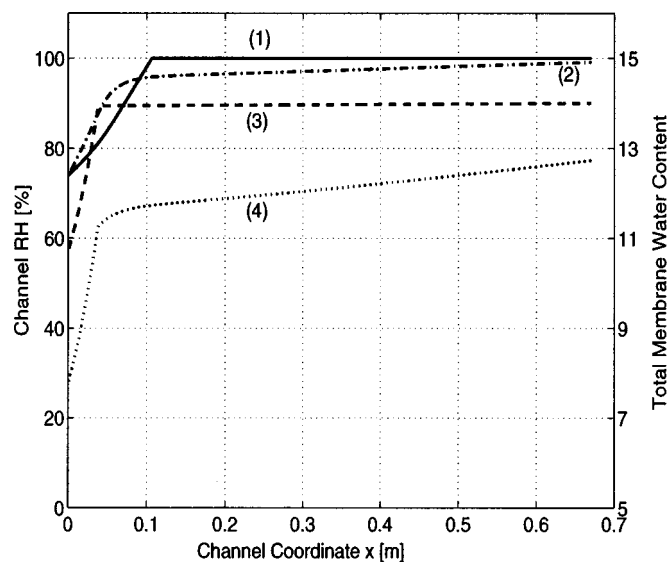

Figure 15. Calculated water concentration profiles in the gas streams and on both sides of the membrane for the fuel coflow configuration (Table III). (1) RH along the cathode flow, (2) RH along the anode flow, (3) and (4), membrane interface water contents at the cathode and anode sides, respectively. While the cathode and anode gas streams saturate rapidly, the anode membrane water content is significantly lower at the inlet than in the counter-flow configuration (see Fig. 8).

for the coflow run compared to the counter-flow run, (see Fig. 8). Figure 14 further clarifies the situation, showing that the computed water transfer is negative (cathode to anode) at the coflow inlet. The water produced at the cathode catalyst sites is brought over to the anode at a rate greater than the osmotic drag, in an attempt to hydrate the anode stream. The water transfer for the counter-flow case is, however, positive at the cathode inlet, where water flows from the relatively humidified anode stream toward the relatively dry cathode stream. The substantial benefit of counter flow is the ability of the two gas streams to even the water management workload, with the saturated outlet end of one gas stream humidifying the opposing stream's relatively dry inlet. Data is not available for low humidification coflow inlets.

Conclusions.—With a simple $1 + 1$ dimensional model for the water management in a PEM FC, and four adjustable parameters, fit to data and then held constant, predictions of long-the-channel water and current distributions can be made over a wide range of operating conditions. A comparison between model results and experimental data suggests that a majority of current production occurs at catalyst sites within the membrane and that oxygen diffusion through membrane water plays a significant role in mass transportation losses. Along-the-channel current distributions suggest that liquid water within the gas diffusion layer has a significant influence on PEM FC operation, even at dry inlet conditions. While the fitted values for the effective oxygen diffusivity are roughly one order of magnitude below its free space value, the effective water diffusivity is almost four orders below the free space value, indicating that water transport from the membrane to the channel, particularly at the dry inlet, is dominated by the nonequilibrium kinetics of the membrane/catalyst sublayer interface.

A Numerical Implementation

The numerical implementation of the model is done in the package MATLAB. The code is an ODE solve embedded in a hierarchy of iterations. The main elements are summarized for coflow and then counter-flow operation below.

Co-flow.—The fundamental computation for coflow operation is an ODE solving for both the anode and cathode fluxes in x from their prescribed values at the inlet to outlet. Equation 4, 5, 14, and 15 represent the vector ODE of the fluxes. In the computations shown in this paper, a grid of 1048 points was used to discretize the length x of the cell and a simple low order explicit stepping technique (forward Euler) was used. For a given cell voltage U, Eq. 49 is an implicit equation for the local current density $I(x)$ that can be solved iteratively given channel concentrations and activities at x that can be determined from the channel fluxes as outlined in the sections on the channel model and the catalyst membrane interface. The diffusive water flux can also be determined from these quantities, Eq. 40. These calculations are embedded inside an external loop which adapts the potential U to achieve the prescribed total current I_T.

Counterflow.—The additional difficulty with computations in counterflow operation is that the vector ODE of the fluxes of Eq. 4, 5, 14, and 15 has data given at different values of x (cathode data at $x = 0$ and anode data at $x = L_c$). Standard shooting techniques, in which the anode outlet conditions (at $x = 0$) are adjusted so that

the coflow computation gives $x = L_c$ anode fluxes that match the target inlet conditions, fail due to the inherent instability associated with integrating against the flow direction in the anode channel. A "back-and-forth shooting" technique was implemented to solve the counter flow problem.[26,27] The anode and cathode fluxes are initially set at their inlet values for all x. The cathode fluxes are then updated using the ODE system in Eq. 4 and 5, solved from $x = 0$ to $x = L_c$ with local current and water transfer computed as described above for co-flow, but using the anode fluxes from the previous iteration. The anode fluxes are then updated, integrating Eq. 14 and 15 from $x = L_c$ to $x = 0$, using the local current and water transfer determined from the previously computed cathode channel values. This process is continued until the anode and cathode flux profiles converge. In the computations shown in this paper, ten iterations were sufficient to have convergence errors of less than 1%.

References

1. D. M. Bernardi and M. W. Verbrugge, *J. Electrochem. Soc.,* **139**, 2477 (1992).
2. T. Berning, D. M. Lu, and N. Djilali, *J. Power Sources,* **106**, 284 (2002).
3. S. Dutta, S. Shimpalee, and J. W. Van Zee, *Int. J. Heat Mass Transfer,* **44**, 2029 (2001).
4. M. Eikerling, Y. I. Kharkats, A. A. Kornyshev, and Y. M. Volfkovich, *J. Electrochem. Soc.,* **145**, 2684 (1998).
5. V. Gurau, F. Barbir, and H. Liu, *J. Electrochem. Soc.,* **147**, 2468 (2000).
6. V. Gurau, H. Liu, and S. Kakac, *AIChE J.,* **44**, 2410 (1998).
7. T. F. Fuller and J. Newman, *J. Electrochem. Soc.,* **137**, 1218 (1993).
8. T. Nguyen and R. White, *J. Electrochem. Soc.,* **140**, 2178 (1993).
9. T. E. Springer, T. A. Zawodzinski, and S. Gottesfeld, *J. Electrochem. Soc.,* **138**, 2334 (1991).
10. T. Thampan, S. Malhotra, H. Tang, and R. Datta, *J. Electrochem. Soc.,* **147**, 3242 (2000).
11. S. Um, C. Y. Wang, K. S. Chen, *J. Electrochem. Soc.,* **147**, 4485 (2000).
12. S. Freunberger, A. Tsukada, G. Fafilek, and F. N. Buechi, *PSI Scientific Report 2002,* V, 94 (2003).
13. V. I. Basura, Ph.D. Thesis, Simon Fraser University, Burnaby, Canada (2000).
14. F. Opekar and D. Svozil, *J. Electroanal. Chem.,* **385**, 269 (1995).
15. I. Rubinstein and B. Zaltzman, *Phys. Rev. E,* **62**, 2238 (2000).
16. G. Xie and T. Okada, *Electrochim. Acta,* **41**, 1569 (1995).
17. T. A. Zawodzinski, J. Davey, J. Valerio, and S. Gottesfeld, *Electrochim. Acta,* **40**, 297 (1995).
18. M. Ottay, Ph.D. Thesis, NTH, Trondheim, Norway (1996).
19. S. Motupally, A. J. Becker, and J. W. Weidner, *J. Electrochem. Soc.,* **147**, 3171 (2000).
20. T. Zawodzinski, C. Derouin, S. Radzinski, R. Sherman, V. Smith, T. Springer, and S. Gottesfeld, *J. Electrochem. Soc.,* **140**, 1981 (1993).
21. P. Futerko and I. M. Hsing, *J. Electrochem. Soc.,* **146**, 2049 (1999).
22. P. Berg and K. Promislow, in *Technical Proceedings of the 2003 Nanotechnology Conference,* Vol. 3, Computational Publications, San Francisco, CA (2003).
23. R. Krishna and R. Taylor, *Multicomponent Mass Transfer,* Chap. 7, Wiley, New York (1993).
24. J. Stumper, S. A. Campbell, D. P. Wilkinson, M. C. Johnson, and M. Davis, *Electrochim. Acta,* **43**, 3773 (1998).
25. J. St. Pierre, D. P. Wilkenson, S. Knights, and M. L. Boss, *J. New Mater. Electrochem. Syst.,* **3**, 99 (2000).
26. T. Eirola, Ph.D. Thesis, Helsinki University of Technology, Helsinki (1985).
27. T. Eirola, *J. Optim. Theory Appl.,* **41**, 599 (1983).